Finite-element simulation of the depolarization factor of arbitrarily shaped inclusions

Abdelilah Mejdoubi and Christian Brosseau*
Laboratoire d'Electronique et Systèmes de Télécommunications, Université de Bretagne Occidentale, CS 93837, 6 avenue Le Gorgeu, 29238 Brest Cedex 3, France
(Received 26 May 2006; revised manuscript received 12 August 2006; published 26 September 2006)

An understanding of the polarization characteristics is a prevailing issue in electrostatics and scattering theory and is also vital to the rational design of future dielectric nanostructures. In this work, a finite-element methodology has been applied to simulate two-phase heterostructures containing a polarizable dielectric inclusion. The inclusions investigated can be considered as arbitrarily shaped cross sections of infinite three-dimensional objects, where the properties and characteristics are invariant along the perpendicular cross-sectional plane. Given the paucity of experimental and numerical data, we set out to systematically investigate the trends that shape and permittivity contrast between the inclusion and the host matrix have on the depolarization factor (DF). The effect of the first–versus second-order concentration virial coefficient on the value of the DF is considered for a variety of inclusion shapes and a large set of material properties. Our findings suggest that the DF for such inclusions is highly tunable depending on the choice of these parameters. These results can provide a useful insight for the design of artificial two-phase heterostructures with specific polarization properties.

DOI: 10.1103/PhysRevE.74.031405 PACS number(s): 61.43.Hv, 77.22.Ej, 77.84.Lf, 68.35.Ct

I. INTRODUCTION

The electromagnetic behavior of heterostructures with controlled size and shape is a maturing subject [1]. It is somewhat alarming then to find that details of the polarization (magnetization) mechanisms of inhomogeneous multiphase granular materials—including quantities such as the polarizability, the depolarization factor (DF), and the magnetizability—remain undetermined for arbitrarily shaped polarizable (magnetizable) entities because this information is a crucial input for theoretical models seeking to describe the dielectric (magnetic) properties of these systems. There are several outstanding challenges in the field that have been only partially addressed [2–5]. For example, how does the DF vary with the shape, size, and orientation of the inclusion? How is the DF affected by the permittivity contrast between the inclusion and the host matrix? What is the influence of dielectric loss on the DF? How should we choose and arrange the inclusion in a given matrix to obtain the largest (or smallest) DF?

We place our work in the context of other related studies. Whereas the calculation of the DF for a few prototypical inclusion geometries that include disk, circular cylinder, elliptical cylinder, sphere, prolate spheroid, and oblate spheroid, has led to a considerable body of theoretical work over the years and has resulted in rigorous solutions [1,6–8], the situation for arbitrarily shaped inclusions is considerably more obscure. To date, a few attempts have focused on the effect of inclusion shape on the DF in heterostructures. In recent works, Weiglhofer [10] and Lakhtakia and Lakhtakia [9] have described procedures for evaluating depolarization dyadics [1,11]. Garboczi and Douglas [12] have shown that the leading-order virial coefficients of diverse properties (permittivity, magnetic permeability) can be expressed in terms of functionals of object shape. Subsequently, on the basis of finite-element (FE) simulations, Sihvola and coworkers [6,13] undertook and presented a procedure for calculating depolarization dyadics of Platonic polyhedra. It has been pointed out recently by Mejdoubi and Brosseau [14–16] that geometrical effects can give rise to significant modifications of the surface-fraction dependence of the effective permittivity. Furthermore, these authors presented simulations showing that the dielectric properties of two-phase particulate heterostructures depend sensitively on the overall shape and perimeter roughness of the inclusion. Other approaches to the dielectric response of systems include real-space renormalization techniques [17] and simulations with networks of resistor-inductor-capacitor (RLC) elements distributed randomly in a plane [18]. In view of the significance of the polarization mechanisms in many contexts in condensed-matter physics, materials science, and other areas in science such as geophysics and biology, there is a well-recognized need to have a quantitative understanding of the DF. It also is important to recall that in the standard electrodynamics theory [19], the DF is introduced as a dyadic (tensor). Full details of the theory can be found in several excellent reviews [11,20–26]. The dyadic $\overleftrightarrow{A}$ depends on the particle shape and not on the dimensions, provided that they remain appreciably smaller than the free-space wavelength, i.e., scale invariance. Parenthetically, it is also interesting to note that the depolarization dyadic is also known as the Polya-Szegö polarization tensor, which appears in problems of potential theory [27,28].

This paper will attempt, in part, to rectify this serious omission from the body of knowledge by investigating a procedure that is capable of allowing the calculation of the DF of polarizable inclusion in heterostructures. The inclu-

*Also affiliated with the Département de Physique, Université de Bretagne Occidentale, Brest Cedex 3, France. Electronic address: brosseau@univ-brest.fr

sions investigated can be considered as arbitrarily shaped cross sections of infinite three-dimensional objects, where the properties and characteristics are invariant along the perpendicular cross-sectional plane. It should be recognized at the outset that the current approach is different from the two-dimensional (2D) systems considered by Barrera *et al.* [4] who focused their attention on the dielectric (optical) response of 2D systems made of identical polarizable entities, such as small conducting particles or molecule, on a flat substrate. In Ref. [4], the influence of a semi-infinite substrate for supported films was taken into account through induced image fields. Since the analytical calculation of the response of an arbitrary composite material is generally intractable, numerical simulation is the standard method to extract the effective properties of these complex media. For that purpose we use a FE methodology to derive the effective permittivity of the mixed medium. As an illustrative application of this technique, we consider a number of systems with different kinds of inclusion geometry and orientation with respect to the applied electric field. One aim of the calculations outlined below is to illustrate how the DF depends on the permittivity ratio between the inclusion and the host matrix. In this study, we devote a significant amount of our efforts to demonstrate that the DF is strongly influenced by the boundaries roughness. This work aims to provide a useful framework for understanding the relationship between the polarization of dielectric heterostructures and morphology in general. A long-term goal of this research is to develop a comprehensive database of DF and polarizability behaviors with a concurrent predictive capability based on numerical models and an expert system. These models will reflect the nature of the inclusion (matrix) interface and the characteristics of the inclusion themselves.

The remainder of this paper is set out as follows. Section II describes some of the technical aspects and details of the computations. Section III reports the results of our calculations, and comments on some of the implications of the results. We review the main conclusions of this study in Sec. IV and discuss some future directions for the continuation of this project. A short appendix contains some explicit calculations about the related issue of three-dimensional cylinders with finite length.

II. METHODOLOGY AND COMPUTATIONAL ASPECTS

We now sketch the analysis that led to our results.

A. Depolarization factor

The dielectric heterostructure is divided into two phases: one phase characterized by different shapes, and isotropic permittivity ε_2 and surface fraction ϕ_2 distributed in another phase characterized by isotropic permittivity ε_1 and surface fraction ϕ_1. Anisotropy can arise out of some asymmetry in the microstructure, e.g., the distribution of oriented nondiscoidal cross section of infinite objects. In the case of the infinite three-dimensional cylinders that we consider, the DF is the tensor

$$\overleftrightarrow{A} = \begin{bmatrix} A_{xx} & A_{xy} & 0 \\ A_{yx} & A_{yy} & 0 \\ 0 & 0 & 0 \end{bmatrix}$$

in a Cartesian system of coordinates. The trace of $\overleftrightarrow{A}$ is unity, and therefore, $0 \leqslant A_{ij} \leqslant 1$, $i=x,y$. For other isotropic cases, the DF is a scalar $\overleftrightarrow{A}=A\overleftrightarrow{1}$. This two-phase composite model has been used in the analysis of a wide variety of problems arising in materials science [29], condensed matter physics [30], geophysics [31], and biosensor applications [32,33] in relation to the problem of connecting the macroscopic properties to its microstructure. For simplicity, the following formulation is written in terms of scalar quantities. However, the procedure is easily generalized by considering permittivity and depolarization tensors.

In many instances the effective permittivity ε can be scaled to collapse to a common set of master curves described by

$$\frac{\varepsilon}{\varepsilon_1} = f\left(\frac{\varepsilon_2}{\varepsilon_1}, \phi_2, A\right), \tag{1}$$

where A $(0 \leqslant A \leqslant 1)$ is a functional of inclusion shape and permittivity ratio only. By now, a broad choice of analytic expressions is available for the function f which may score very well if compared to experimental or numerical data [1,6,7,29,33–36]. For example, the Maxwell Garnett (MG) [1,6,7,29] form for f is given by

$$f\left(\frac{\varepsilon_2}{\varepsilon_1}, \phi_2, A\right) = 1 + \frac{\phi_2\left(\frac{\varepsilon_2}{\varepsilon_1} - 1\right)}{1 + A(1-\phi_2)\left(\frac{\varepsilon_2}{\varepsilon_1} - 1\right)}. \tag{2}$$

Note that the roles of host and inclusion in Eq. (2) are not reciprocal. In other instances, the function f appearing in the right-hand side of Eq. (4) is more complex, e.g., for Böttcher equation [also termed symmetric Bruggeman, (SBG)] [1,6,7,29], it can be computed as

$$f\left(\frac{\varepsilon_2}{\varepsilon_1}, \phi_2, A\right) = \frac{1 - A\left(1 + \frac{\varepsilon_2}{\varepsilon_1}\right) + \phi_2\left(\frac{\varepsilon_2}{\varepsilon_1} - 1\right) \pm \sqrt{\left[1 - A\left(1 + \frac{\varepsilon_2}{\varepsilon_1}\right) + \phi_2\left(\frac{\varepsilon_2}{\varepsilon_1} - 1\right)\right]^2 + 4A(1-A)\frac{\varepsilon_2}{\varepsilon_1}}}{2(1-A)}. \tag{3}$$

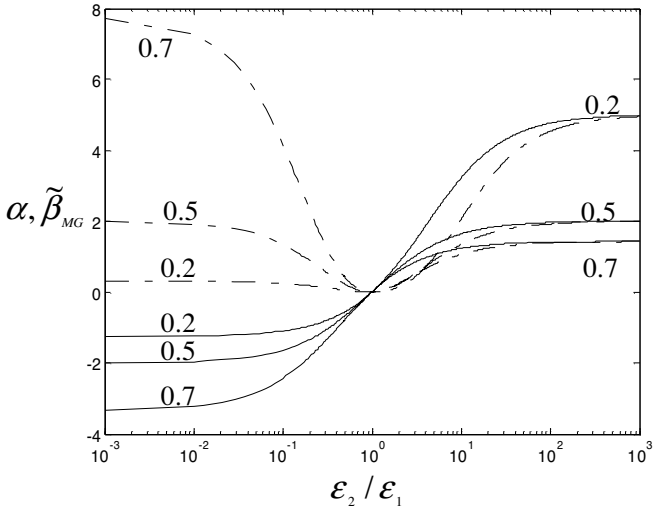

FIG. 1. Plot of α and β_{MG} vs $\varepsilon_2/\varepsilon_1$ for a selection of DF. The dashed (respectively, solid) line represents α (respectively, $\tilde{\beta}_{\mathrm{MG}}$).

Note that the roles of host and inclusion media are reciprocal. In this way of thinking the procedure amounts to finding the roots of a second-order polynomial and the physical root of Eq. (3) is determined from requirements of positivity of ε (or of the imaginary part, ε'', of ε corresponding to dissipation). However, the dipolar nature of MG and SBG approaches fundamentally limits the range of applicability of Eqs. (2) and (3) [37,38]. In practice, laboratory or numerical data can be approximated arbitrarily accurately with Eq. (2) or Eq. (3) only in the dilute limit, i.e., when ϕ_2 is sufficiently small.

We emphasize that, on the experimental or numerical side, it is customary of the MG and SBG equations that data are first confronted, and on the theoretical side, models of increasing complexity are regularly investigated within the MG and SBG frameworks as a means to unveil potential new phenomena. The question now is whether the MG and SBG analyses give different sets of A values. At the heart of this study, A enters a linearized version of Eq. (1) as a fitting parameter. For the dilute limit we expanded Eqs. (2) and (3) to first order in ϕ_2. In its simplest form, this series expansion is

$$f\left(\frac{\varepsilon_2}{\varepsilon_1}, \phi_2, A\right) = 1 + \alpha\phi_2 + O(\phi_2^2), \tag{4}$$

where $\alpha_{\mathrm{MG}}=\alpha_{\mathrm{SBG}}=\alpha=1/[A+1/(\varepsilon_2/\varepsilon_1-1)]$. This expression leads to three results. First, we show that the leading first-order corrections are similar for MG and SBG equations. Thus, the value of A we obtain is, up to the level of approximation based on the dilute limit, model independent. Second, Eq. (4) allows the determination of A, which is independent of ϕ_2. Third, one should note that in the limit $\varepsilon_2/\varepsilon_1 \to \infty$, $\alpha \to 1/A=\alpha^{\infty}$. Obviously, in this case, there are no effects due to the permittivity contrast since the electric field is ideally screened by the dielectric interfaces. By way of illustration and to give some orders of magnitude, we plot α as a function of $\varepsilon_2/\varepsilon_1$ for different values of the DF in Fig. 1. Others have used this approach to look at the functionals of shape associated with the solution of the Laplace and the Navier-Stokes equations on the exterior of objects having general shape by examining virial coefficients of diverse properties [12] or by considering asymptotic models of dilute composites [28].

Before examining the trends of the DF, it is instructive to look at the series expansion to second order in ϕ_2. The second-order expansion of f may be written as

$$f\left(\frac{\varepsilon_2}{\varepsilon_1}, \phi_2, A\right) = 1 + \tilde{\alpha}\phi_2 + \tilde{\beta}\phi_2^2 + O(\phi_2^3), \tag{5}$$

with coefficients

$$\tilde{\beta}_{\mathrm{MG}} = \frac{1}{A + \dfrac{2}{\dfrac{\varepsilon_2}{\varepsilon_1} - 1} + \dfrac{1}{A}\left(\dfrac{1}{\dfrac{\varepsilon_2}{\varepsilon_1} - 1}\right)^2}$$

and

$$\tilde{\beta}_{\mathrm{SBG}} = \frac{\dfrac{\varepsilon_2}{\varepsilon_1}}{A^2\left(\dfrac{\varepsilon_2}{\varepsilon_1} - 1\right)\left(1 + \dfrac{1}{A\left(\dfrac{\varepsilon_2}{\varepsilon_1} - 1\right)}\right)^3}$$

obtained using the computer package, MAPLE. Thus, at higher than linear order approximation, the A values are model dependent and can differ from those determined by using the first-order approximation depending on the range of ϕ_2, which is considered. In general, this comparison depends on the system under consideration and the level of accuracy required. Such an effect will be discussed in this work. For the purposes of the present discussion, the DF will be analyzed by fitting the effective permittivity data by means of Eq. (4) for $\phi_2 < \phi_{2co} \approx 0.05$, or using Eq. (5) for $\phi_2 < \phi_{2co} \approx 0.10$. It turns out that $\tilde{\beta}_{\mathrm{MG}} \to 1/A=\tilde{\beta}^{\infty}$ (see Fig. 1), while $\tilde{\beta}_{\mathrm{SBG}} \to 1/A^2=(\tilde{\beta}^{\infty})^2$ in the limit $\varepsilon_2/\varepsilon_1 \to \infty$. The rest of this section is devoted to a discussion of the FE analysis and the computational details of using it in ε and DF calculations.

B. Finite-element methodology

Each inclusion can be viewed as an infinite cylinder with a cross section of surface Ω and axis along the z axis embedded in an infinite medium for which the transverse effective permittivity ε depends on (x,y) only. Solving the problem at hand means finding expressions for the scalar potential V and electric field $\mathbf{E}=-\nabla V$ everywhere within the domain Ω in which there is no source charge. The local potential distribution inside Ω is given by the conservation of electric displacement flux through the "surface" S, i.e., Laplace partial-differential equation

$$\nabla \cdot [\varepsilon(\mathbf{r})\, \nabla V] = 0, \tag{6}$$

where $\varepsilon(\mathbf{r})$ and V are the local permittivity and potential, respectively. In the case at hand, the effective permittivity

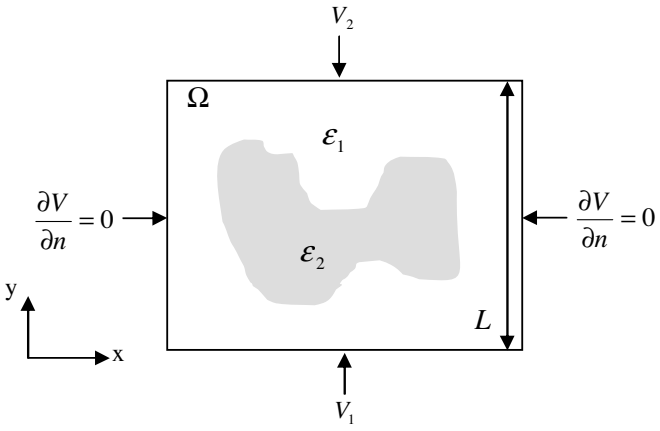

FIG. 2. Cartoon sketch of the unit-square cell of a typical composite structure containing a single inclusion (shaded region). The inclusion shape can be considered as the cross section of an infinite three-dimensional object where the properties and characteristics are invariant along the perpendicular to the cross-sectional plane. The model space can simulate a capacitor by applying a potential difference between the top and bottom faces of the model space. The evaluation of the effective permittivity, along the direction corresponding to the applied field, i.e., $\varepsilon=\varepsilon_y$, requires that the conservation of the electric-displacement flux through the surface S has to be solved subject to appropriating the relevant boundary conditions for the potential. We fix $V_1=0$ V and $V_2=1$ V and assume that $\partial V/\partial n=0$ on the other side faces. L and S have both been set to unity.

along the direction corresponding to the applied field, i.e., $\varepsilon=\varepsilon_y$, is found by integration via $\int_S \varepsilon_1(\partial V/\partial n)_1=\varepsilon(V_2-V_1)/LS$, where V_2-V_1 denotes the difference of potential imposed in the y direction, L is the composite thickness in the same direction, and S is the surface of the unit cell perpendicular to the applied field. The potential on the top face of the square, V_2, is fixed at a value of 1 V, while that on the bottom face, V_1, is fixed at 0 V (Fig. 2). One then solves Eq. (6) subject to appropriate boundary conditions.

Once we have stated the mathematical equation that defines the physics of the system, i.e., Eq. (6), we must figure out how to solve this equation for the particular domain we are interested in. The principle of the FE simulation method for solving Eq. (6) is to break up the continuous domain Ω into discrete elements to form a finite-dimensional subspace and approximate Eq. (6) by an algebraic expression, which references adjacent grid points [39]. In the FE method, the domain can be discretized into a number of uniform or nonuniform finite elements that are connected via nodes. The change of V with regard to spatial position is approximated within each element by an interpolation function. The original boundary-value problem is then replaced with an equivalent integral formulation. The interpolation functions are then substituted into the integral equation, integrated, and combined with the results from all other elements in the domain Ω. Then, the results of this procedure are transformed into a matrix equation, which is subsequently solved for V. The algorithm was similar to that used in Ref. [16]. More details on the merits and the implementation of the algorithm can be found in our previous work [16].

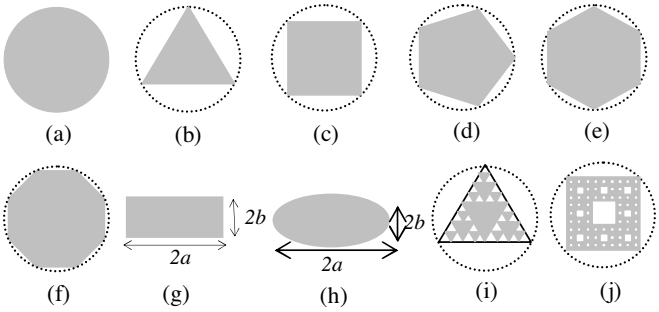

FIG. 3. Schematic diagrams of the structural motifs of the inhomogeneous mixtures considered in this work: (a) disk, (b) equilateral triangle, (c) square, (d) regular pentagon, (e) regular hexagon, (f) regular octagon, (g) rectangle of dimensions $2a$ and $2b$, (h) ellipse of semimajor axis a and semiminor axis b, (i) Sierpinski triangle (third iteration), (j) Sierpinski square (third iteration).

For simplicity, we will focus our discussion on deterministic two-phase heterostructures. In all cases, the simulation cell Ω is a square of length $L=1$. As a side note, we do point out that we verified that if one of the two dimensions of the simulation box is significantly longer than the other one, e.g., the rectangular cell (1×2) instead of the unit-square cell, does not influence the permittivity and DF values. Periodic boundary conditions are enforced in the x direction for these structures. All data were obtained using the FE element as implemented in the commercial finite-element solver COMSOL MULTIPHYSICS® and the procedure sorted out ε on a personal computer (PC) with a Pentium IV processor (3 GHz). COMSOL MULTIPHYSICS permits the closely controlled generation of FE meshes through the use of input files containing complete instructions for node-by-node and element-by-element mesh specification, along with imposition of boundary conditions. In this work, the y axis was defined as pointing in the direction of the applied electric field. For reasons described above, we devote a significant amount of our efforts to studying the properties and trends of the DF tensor by rotating the inclusion with respect to the y axis.

Before proceeding, it is useful first to present in Fig. 3 the relatively simple prototypical types of cross section of infinite three-dimensional objects that were selected in this study: regular n-gons, ellipse, rectangle, Sierpinski square, and triangle fractal structures. Symmetric objects such as polygons are of special interest because their geometric properties can be predicted by using irreducible representations of their symmetry groups [40]. Fractal particles are of interest for interrogating fundamental questions such as packing, porosity, as well as for applications in biological and nanoscale systems [15,41,42]. In a previous report [15], we have shown that the effective permittivity of deterministic fractal patterns changes with reduced perimeter according to a similarity transformation. The ellipse is characterized with semimajor axis a and semiminor axis b. The dimensions of the rectangle are $2a\times 2b$.

TABLE I. Summary of the DFs for polygons. The letter between the brackets refers to the different geometries represented in Fig. 2. The column labeled 1 contains DF first-order values determined by using Eq. (4); the column labeled 2 contains the DF values for the second-order approximation using the MG equation. The cutoff values of ϕ_2, ϕ_{2co}, to obtain the DF by using Eq. (4) or (5), is also specified. To fix the notation we consider one specific orientation ($\theta=0°$) with respect to the direction of the applied electric field.

	Inclusion							
	$A\left(\frac{\epsilon_2}{\epsilon_1}=\frac{20}{2}\right)$		$A\left(\frac{\epsilon_2}{\epsilon_1}=\frac{2000}{2}\right)$		$A\left(\frac{\epsilon_2}{\epsilon_1}=\frac{1}{100}\right)$		ϕ_{2co}	
Approximation	1	2	1	2	1	2	1	2
Disk [a]	0.482	0.497	0.482	0.497	0.482	0.503	0.049	0.102
Equilateral triangle ([b] $\theta=0°$)	0.392	0.401	0.368	0.374	0.590	0.626	0.050	0.108
Square ([c] $\theta=0°$)	0.447	0.461	0.438	0.451	0.523	0.549	0.051	0.109
Regular pentagon ([d] $\theta=0°$)	0.464	0.478	0.460	0.473	0.501	0.526	0.050	0.108
Regular hexagon ([e] $\theta=0°$)	0.471	0.487	0.469	0.484	0.493	0.516	0.051	0.104
Regular octogon ([f] $\theta=0°$)	0.477	0.493	0.476	0.491	0.486	0.509	0.052	0.107

A natural step in the development of numerical methods is to benchmark and test the proposed methods against a selected set of theoretical or experimental data, which allows one to assign a targeted error range of predictivities. As noted in the Introduction, despite concentrated efforts, very few exact results on the DF are known. The only data to which to compare our calculated DF are the values given by Garboczi and Douglas [12] for the n-gons inclusion, which are in good agreement with our value (see below).

III. RESULTS AND DISCUSSION

The results for the numerical estimates of A (or Cartesian components of $\overleftrightarrow{A}$) are summarized in Tables I–VII. Before we proceed to the discussion of the DF data, we would like to note that best-fit parameters for DF obtained either by using a first-order approximation, i.e., Eq. (4), or a second-order approximation, i.e., Eq. (5), have shown to produce similar results (within numerical uncertainty). Unless other-

TABLE II. Summary of the DFs for the ellipse. The electric field is y polarized. The lines correspond to different values of the aspect ratio.

	Ellipse ([h] $\theta=0°$) y polarized							
	$A\left(\frac{\epsilon_2}{\epsilon_1}=\frac{20}{2}\right)$		$A\left(\frac{\epsilon_2}{\epsilon_1}=\frac{1}{100}\right)$		$A(\epsilon_2=20-j100, \epsilon_1=2-j0)$			
					ϵ'		ϵ''	
Approximation	1	2	1	2	1	2	1	2
$a/b=7$	0.859	0.901	0.863	0.881	0.864	0.901	0.864	0.900
$a/b=5$	0.817	0.864	0.817	0.854	0.820	0.867	0.817	0.861
$a/b=3$	0.732	0.772	0.732	0.773	0.732	0.772	0.732	0.770
$a/b=3/2$	0.582	0.607	0.582	0.609	0.582	0.606	0.582	0.604
$a/b=1$ (disk)	0.482	0.497	0.482	0.503	0.482	0.499	0.482	0.496
$a/b=2/3$	0.381	0.389	0.381	0.393	0.381	0.388	0.381	0.387
$a/b=1/3$	0.230	0.221	0.230	0.224	0.230	0.233	0.230	0.232
$a/b=1/5$	0.155	0.152	0.147	0.138	0.155	0.153	0.157	0.160
$a/b=1/7$	0.120	0.120	0.120	0.120	0.120	0.120	0.120	0.120

TABLE III. Same as in Table II for the ellipse. The electric field is x polarized. The lines correspond to different values of the aspect ratio.

	Ellipse ([h] $\theta=0°$) x polarized							
	$A\left(\frac{\epsilon_2}{\epsilon_1}=\frac{20}{2}\right)$		$A\left(\frac{\epsilon_2}{\epsilon_1}=\frac{1}{100}\right)$		$A(\epsilon_2=20-j100, \epsilon_1=2-j0)$			
					ϵ'		ϵ''	
Approximation	1	2	1	2	1	2	1	2
$a/b=7$	0.118	0.119	0.117	0.111	0.119	0.120	0.119	0.120
$a/b=5$	0.155	0.152	0.147	0.143	0.153	0.158	0.158	0.158
$a/b=3$	0.231	0.235	0.231	0.236	0.235	0.240	0.238	0.238
$a/b=3/2$	0.382	0.389	0.382	0.393	0.382	0.382	0.384	0.390
$a/b=1$ (disk)	0.482	0.497	0.481	0.503	0.482	0.499	0.482	0.496
$a/b=2/3$	0.582	0.605	0.584	0.608	0.583	0.605	0.583	0.604
$a/b=1/3$	0.733	0.762	0.733	0.764	0.738	0.760	0.738	0.759
$a/b=1/5$	0.818	0.855	0.823	0.844	0.818	0.855	0.818	0.857
$a/b=1/7$	0.859	0.908	0.866	0.886	0.860	0.905	0.861	0.903

wise noted, the DF values plotted in the figures are those obtained using Eq. (5).

A. Effect of varying the inclusion (cross-section) shape and orientation with respect to the applied electric field

Consider first the case of polygons (Fig. 4 and Table I). Remarkably, we found a general trend in the series of polygons, i.e., the values of A are substantially higher as the number of vertices of the inclusion increases when, respectively, $\varepsilon_2/\varepsilon_1>1$. Overall, this trend appears to be independent of the permittivity ratio over the range of permittivity ratios considered. Clearly, this is a large effect that cannot be neglected in considering depolarization properties of these inclusions [43]. For polygons, A achieves its absolute maxi-

TABLE IV. Same as in Table II for the ellipse. The electric field is y polarized. The aspect ratio is $a/b=1/3$. The lines correspond to different values of the angle θ of rotation of the inclusion with respect to the y axis.

	Ellipse ([h] $a/b=1/3$) y polarized							
	$A\left(\frac{\epsilon_2}{\epsilon_1}=\frac{20}{2}\right)$		$A\left(\frac{\epsilon_2}{\epsilon_1}=\frac{1}{100}\right)$		$A(\epsilon_2=20-j100, \epsilon_1=2-j0)$			
					ϵ'		ϵ''	
Approximation	1	2	1	2	1	2	1	2
0°	0.230	0.221	0.230	0.224	0.230	0.233	0.230	0.232
15°	0.246	0.246	0.315	0.317	0.252	0.252	0.251	0.251
30°	0.292	0.292	0.472	0.485	0.288	0.291	0.277	0.277
45°	0.377	0.384	0.600	0.626	0.368	0.370	0.328	0.329
60°	0.508	0.523	0.679	0.708	0.493	0.498	0.425	0.427
75°	0.658	0.686	0.725	0.748	0.655	0.664	0.598	0.603
90°	0.732	0.772	0.732	0.773	0.732	0.772	0.732	0.770
105°	0.658	0.686	0.725	0.748	0.655	0.664	0.598	0.603
120°	0.508	0.523	0.679	0.708	0.493	0.498	0.425	0.427
135°	0.377	0.384	0.679	0.708	0.368	0.370	0.328	0.329
150°	0.292	0.292	0.472	0.485	0.288	0.291	0.277	0.277
165°	0.292	0.292	0.472	0.485	0.288	0.291	0.277	0.277
180°	0.230	0.221	0.230	0.224	0.230	0.233	0.230	0.232

TABLE V. Summary of the DFs for the Sierpinski triangle. The electric field is y polarized. The lines correspond to different values of the iteration number.

	Sierpinski triangle $A\left(\frac{\varepsilon_2}{\varepsilon_1}=\frac{20}{2}\right)$		Sierpinski triangle $A\left(\frac{\varepsilon_2}{\varepsilon_1}=\frac{1}{100}\right)$		Sierpinski triangle $A(\varepsilon_2=20-j100,\varepsilon_1=2-j0)$			
	Approximation		Approximation		Approximation		Approximation	
Iteration number	1	2	1	2	1	2	1	2
0	0.392	0.401	0.590	0.626	0.370	0.376	0.325	0.330
1	0.268	0.269	0.695	0.718	0.279	0.284	0.288	0.289
2	0.173	0.171	0.774	0.793	0.209	0.211	0.249	0.250
3	0.099	0.099	0.833	0.848	0.155	0.154	0.215	0.215
4	0.044	0.043	0.876	0.892	0.113	0.112	0.185	0.185

mum for disk when, respectively, $\varepsilon_2/\varepsilon_1>1$, i.e., $A\to 1/2$ in the limit $n\to\infty$. It was verified (not shown) that DF is θ independent, where θ denotes an angle of orientation of the inclusion with respect to the electric field (y polarized), in agreement with the symmetry properties of polygons [40]. A comparison of the two approximations, i.e., Eqs. (4) and (5), indicates that while there are slight differences in the actual values, the resulting DFs are comparable (Table I). It is difficult to decide which of these procedures provides the better description in general. The data from Garboczi and Douglas [12] are presented for comparison. They are close to the current results.

The effect of anisotropic inclusions, i.e., ellipse and rectangle, for an electric field polarized in the x and y directions are summarized in Tables II and III. As displayed in Fig. 5, there is a significant effect of inclusion asymmetry on DF. The identical mild "S"-shaped profile is observed for both inclusions. For the purpose of comparison, we plot the DF tensor components for two polarizations in Fig. 5. From this graph and Tables II and III, one directly verifies that $\mathrm{tr}(\overleftrightarrow{A})=1$. In Fig. 5, the data point for the rectangle drops somewhat below the data corresponding to the ellipse. The origin of this difference stems from the roundness of the inclusion. Our simulation indicates that a difference of about one order of magnitude can be evidenced between the longitudinal and transverse DFs. But even more remarkable is the effect of the orientation of the ellipse and the rectangle with respect to the applied electric field, qualitatively almost identical for both inclusions (Table IV). This is illustrated in Fig. 6, where we found that the angular dependence of DF is well represented by a $\sin(\theta)$ law. Interestingly, we have also found that the angular variations in DF displayed in Fig. 6 provide information about the issue of an equivalent disk for polarized bodies of anisotropic shape. For example, if we set $\varepsilon_2/\varepsilon_1=20/2$ and $a/b=1/3$, as the rectangle and ellipse are rotated about an axis parallel to the applied electric field at 60° and 120°, the DF is nearly equal to the disk value.

For comparison and completeness, we have undertaken further calculations on fractal inclusions. The same simulations were run using the same set of parameters for the first four iterations of the fractal patterns. This is illustrated in Tables V and VI for the Sierpinski triangle and square, respectively. One outstanding issue from previous investigations of heterostructures containing fractal inclusion [15] is whether there is a dependence of the DF on the iteration number. Figures 7 and 8 suggest that, for a sufficiently large iteration number, the DFs converge either to 0 or to 1.

TABLE VI. Same as in Table V for the Sierpinski square.

	Sierpinski triangle $A\left(\frac{\varepsilon_2}{\varepsilon_1}=\frac{20}{2}\right)$		Sierpinski triangle $A\left(\frac{\varepsilon_2}{\varepsilon_1}=\frac{1}{100}\right)$		Sierpinski triangle $A(\varepsilon_2=20-j100,\varepsilon_1=2-j0)$			
	Approximation		Approximation		Approximation		Approximation	
Iteration number	1	2	1	2	1	2	1	2
0	0.447	0.461	0.523	0.549	0.439	0.452	0.418	0.430
1	0.393	0.396	0.580	0.603	0.393	0.401	0.402	0.406
2	0.337	0.337	0.628	0.651	0.346	0.352	0.376	0.381
3	0.283	0.285	0.667	0.691	0.309	0.310	0.355	0.357
4	0.235	0.235	0.711	0.725	0.270	0.274	0.336	0.337

TABLE VII. Same as in Table I for complex permittivity. ε' and ε'' denote the real and imaginary part of the effective permittivity, respectively.

	Inclusion							
	$A(\varepsilon_2=2-j100,\varepsilon_1=2-j0)$				$A(\varepsilon_2=20-j100,\varepsilon_1=2-j0)$			
	ε'		ε''		ε'		ε''	
Approximation	1	2	1	2	1	2	1	2
Disk [a]	0.482	0.497	0.482	0.496	0.482	0.499	0.482	0.496
Equilateral triangle ([b] $\theta=0°$)	0.369	0.375	0.324	0.329	0.370	0.376	0.325	0.330
Square ([c] $\theta=0°$)	0.438	0.451	0.418	0.429	0.439	0.452	0.418	0.430
Regular pentagon ([d] $\theta=0°$)	0.460	0.473	0.449	0.461	0.463	0.477	0.460	0.472
Regular hexagon ([e] $\theta=0°$)	0.469	0.484	0.463	0.476	0.473	0.488	0.463	0.477
Regular octagon ([f] $\theta=0°$)	0.476	0.491	0.473	0.487	0.476	0.491	0.473	0.487

B. Effect of varying permittivity contrast ratio

To further investigate our findings, the same systems were subjected to different permittivity contrast between the constituent materials. All other parameters were unaltered. Specifically, we consider a set of situations corresponding to small and large permittivity contrast ratio $\varepsilon_2/\varepsilon_1$. Table I summarizes all numerical results for polygons. On examining the data in Table I and those plotted in Fig. 4, we observe that an absolute minimum (respectively, maximum), corresponding to the case of a disk, for DF is obtained when $\varepsilon_2/\varepsilon_1<1$ (respectively, $\varepsilon_2/\varepsilon_1>1$). Moreover, the values of A are substantially lower (respectively, higher) as the number of vertices of the inclusion increases when $\varepsilon_2/\varepsilon_1<1$ (respectively, $\varepsilon_2/\varepsilon_1>1$). This effect can be interpreted as being due to the Keller-Dykhne duality (or phase exchange) relation [7,8,15,29], i.e., $\varepsilon(\varepsilon_1,\varepsilon_2)\varepsilon(\varepsilon_2,\varepsilon_1)=\varepsilon_1\varepsilon_2$, which implies that $A\leftrightarrow 1-A$ when $\varepsilon_1\leftrightarrow\varepsilon_2$. The data clearly show a more pronounced trend with increasing the permittivity contrast between the inclusion and the embedding matrix. We ascribe this difference to the larger change in the local electric field.

As another illustration of these calculations, the results for the ellipse are tabulated for $\varepsilon_2/\varepsilon_1\gg 1$ and $\varepsilon_2/\varepsilon_1\ll 1$ as a function of the aspect ratio a/b in Table II. We observe that the DF along the direction parallel to the electric field is very similar for the two selected permittivity ratios. An interesting

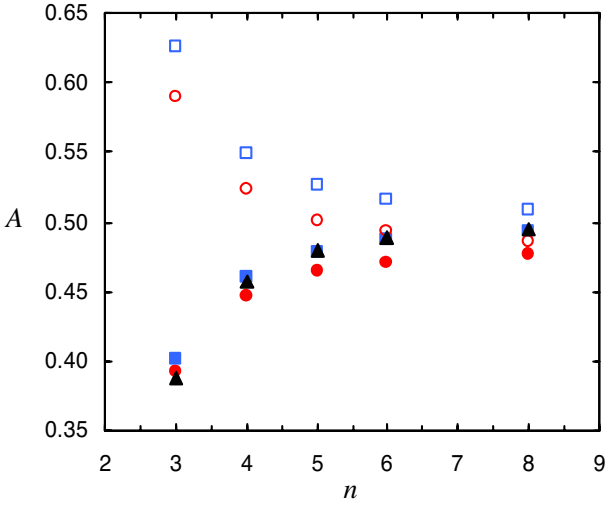

FIG. 4. (Color online) Number of vertices dependence of the DF for polygons. Open circles and squares correspond to the values of A deduced from first-order and second-order approximation, respectively, for $\varepsilon_2/\varepsilon_1=20/2$, whereas solid circles and squares correspond to the values of A deduced from first-order and second-order approximation, respectively, for $\varepsilon_2/\varepsilon_1=1/100$. For comparison, the DF data (solid triangles) of Garboczi and Douglas [12] are also shown for polygons in the limit $\varepsilon_2/\varepsilon_1\to\infty$.

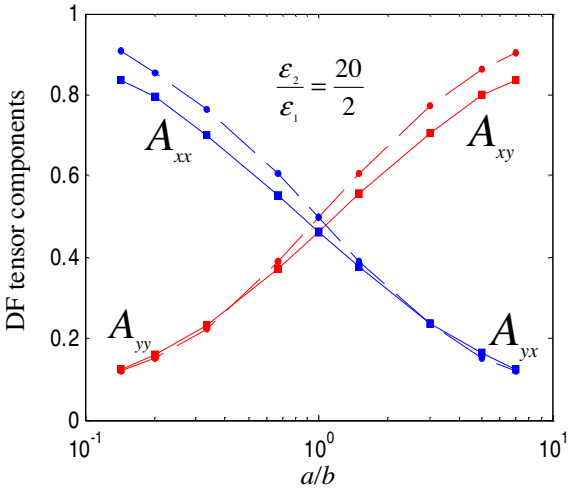

FIG. 5. (Color online) Aspect-ratio dependence of the DF tensor components for ellipse (●) and rectangular (■) inclusion displayed on a semilogarithmic plot. $\varepsilon_2/\varepsilon_1=20/2$. The lines are guides for the eyes.

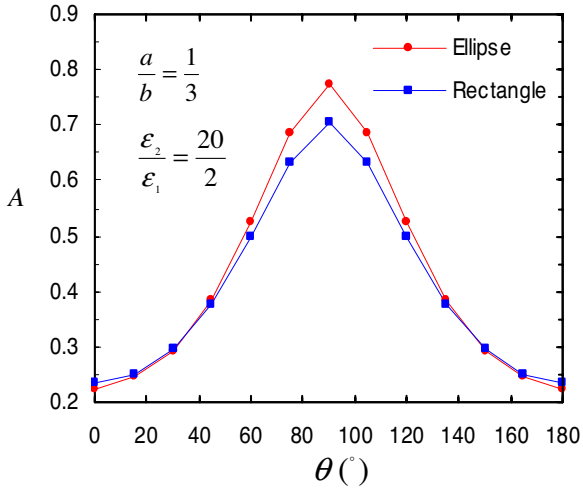

FIG. 6. (Color online) A plot of the angular dependence of the DF. Inclusion rotations are performed about the y axis. The symbols are (●) ellipse, and (■) rectangle. The permittivity contrast is set to $\varepsilon_2/\varepsilon_1=20/2$ and the aspect ratio is $a/b=1/3$. The lines are guides for the eyes.

feature is that $A(\varepsilon_2/\varepsilon_1<1)$ is always larger than $A(\varepsilon_2/\varepsilon_1>1)$ for a given value of the aspect ratio. According to the results summarized in Table VI, the sin θ law is confirmed by a similar plot (not shown) for data corresponding to $\varepsilon_2/\varepsilon_1<1$.

Subsequently, the focus of our attention has been on Sierpinski fractal inclusions. The results in Figs. 7 and 8 and in Tables V and VI suggest two different and opposite trends for this type of inclusion. As before, this behavior originates from the duality symmetry. Moreover, it is found that $A(\varepsilon_2/\varepsilon_1\ll 1)\to 1$ and $A(\varepsilon_2/\varepsilon_1\gg 1)\to 0$ at a large iteration number.

C. Impact of dielectric losses

So far, we have considered lossless materials in our calculations. For all practical structures, material loss is a major

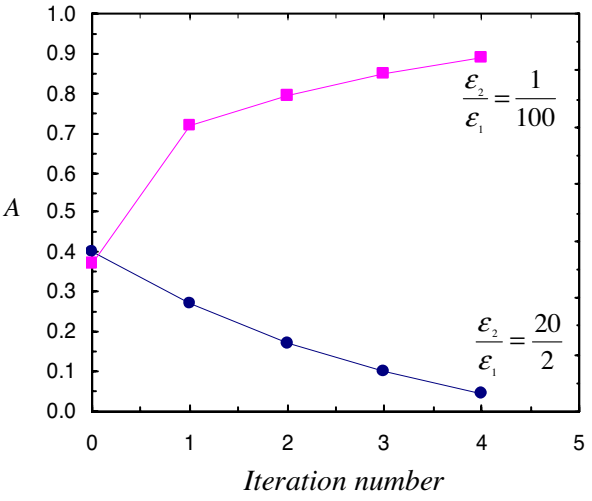

FIG. 7. (Color online) Iteration-number dependence of DF for the Sierpinski triangle. The full circles correspond to $\varepsilon_2/\varepsilon_1=20/2$ and full squares to $\varepsilon_2/\varepsilon_1=1/100$. The lines are guides for the eyes.

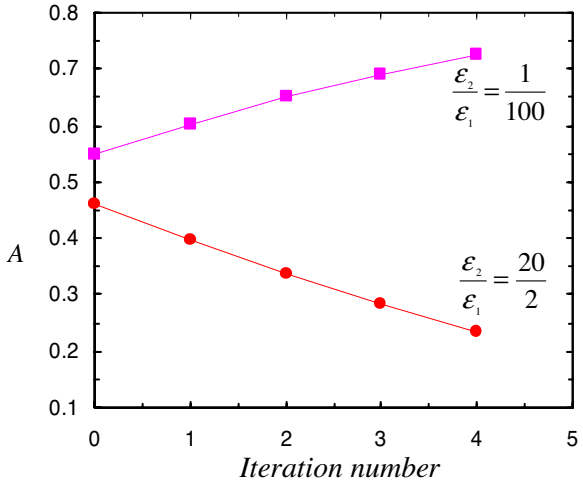

FIG. 8. (Color online) Same as in Fig. 7 for the Sierpinski square.

issue. In this subsection, the impact of complex permittivity on the A values is discussed. By considering first polygons, two important trends are observed. Firstly, we can see in Table VII that the values of A bear strong resemblance to the case of lossless polygons. Indeed on closer examination of the similarity between in DF for lossless polygons and the corresponding lossy polygons, we find a similar correlation with the number of vertices as displayed in Fig. 4. Secondly, it should be emphasized that the same value of A can be obtained from either the real or the imaginary parts of the effective permittivity for the two sets of $(\varepsilon_1,\varepsilon_2)$ values investigated (Table VII). For purposes of comparison and because it is germane to discussions of the effective tensorial properties of bodies of anisotropic shape, the DF is also given in Tables II and III for the ellipse. As we can see in these tables, the DF determined from the real part of the effective permittivity, is in general, closer to the value of A determined for lossless inclusions. An effect similar to the one described above has been observed in the case of lossy fractal inclusions, however, with much more significant differences with the lossless case (Tables V and VI).

D. Discussion

It is worth discussing some features of the calculations summarized in Tables I–VII. This simple analysis shows how the presence of an arbitrarily shaped inclusion in a two-phase composite structure can induce changes in the DF, which in turn translate into changes of the dielectric properties of the material. Collectively, these data are consistent with the earlier numerical data of Garboczi and Douglas [12]. However, as stated previously, we are aware of no closed-form analytic expressions of the DF of dielectric objects of complex shapes with which we can compare our data in the general case.

Our results raise important questions and implications of the effect of symmetry on the polarization properties of dielectric structures. Just as the rotational symmetry of polygons is accompanied by invariance of the DF under discrete rotation, duality (phase-interchange relation) symmetry has a

strong impact on the dielectric behavior of inclusion with anisotropic shape [7,8,15,29].

Another important point has to do with the questions as to what parameters determine the lowest (or highest) DF on particular types of inclusion constrained to sit in a circumscribed disk, and of an equivalent disk for polarized bodies of arbitrary shape, which is determined by imposing the equality between the DFs of the two shapes. This idea was exploited in a recent work [44] concerned with the magnetostatic equivalence for magnetized bodies of arbitrary shape. Another observation is that the S-shaped form commented upon above is similar with the analysis of Jones and Friedman [45] for ellipsoids.

The current results should be relatively general in that they were inferred from a minimalistic model of the permittivity of the composite structure, i.e., dilute limit. This model can be used as a valuable tool to guide the experimental efforts in the quest for more efficient materials with tailored and/or substantially enhanced polarization properties.

Previous studies from our group on fractal inclusions have revealed the importance of scale invariance on their dielectric properties [14–16]. For these Sierpinski-type geometries constrained to sit in a circumscribed disk, the perimeter becomes infinitely large as the iteration number of the fractal pattern $\rightarrow\infty$, while the surface area $\rightarrow 0$. This leads to an example of a dielectric object of complex shape whose DF can be much smaller than the DF of the disk containing the object.

As has been suggested by a referee, we discuss in the Appendix the calculation of the DF of a three-dimensional dielectric circular column with finite length for a wide range of the length-to-radius ratio. The purpose of this calculation was to emphasize once again that the inclusions that we considered are not representative of "two-dimensional inclusions" and cannot be trivially studied by neglecting the third dimension or by making it equal to zero. For instance, a "disk" cannot be obtained thinking of a three-dimensional cylinder with a negligible length. On the contrary, the shapes investigated, and shown in Figs. 2 and 3, have to be considered as cross sections of infinite three-dimensional objects.

Having said this, we briefly mention that it is worth discussing the above findings in relation to previous work on the computation of the demagnetizing factors for a uniformly magnetized inclusion with an arbitrary shape. In the present paper we have specialized the language to permittivity. For reasons of mathematical analogy, the results of this study translate immediately into equivalent results for the magnetic permeability of such mixed media. Although this issue has been studied extensively for 3D objects (ellipsoid), notably by Stoner [46] and Osborne [47], quantitative predictions for 2D inclusions of arbitrary shape are scarce. However, Tandon and co-workers [48] showed that it is affordable to evaluate the demagnetization tensor of quasi-2D inclusions with the method of Fourier-space representation of the inclusion shape. Their formalism can also be applied to the computation of the magnetostatic self-energy for a particle with an arbitrary shape.

IV. CONCLUDING REMARKS

In summary, this paper represents a systematic FE study of DF in two-phase heterostructures. Our goal in the research described in the previous sections has been to address the relationship between the DF and the shape of inclusion, what permittivity contrast between the inclusion and the host matrix determines the lowest (or highest) DF on particular types of inclusion, and the trend in DF for polygons as a function of the number of vertices. Both lossless and absorbing inclusions were considered. The method inherently takes into account the tensorial character of dielectric response in heterostructures. Specific findings of the developments presented here are as follows.

(1) When combined with other work, the present results for a series of dielectric objects indicate that the DF can be finely tuned depending on the object's shape, the permittivity contrast between the inclusion and the embedding matrix, and the orientation of the inclusion with respect to the applied electric field.

(2) We have established that the trend in DF for polygons correlates well with the number of vertices.

(3) Our calculations also provide information about the issue of an equivalent disk for polarized bodies of anisotropic shape. Although the above examples serve to illustrate the richness of depolarization behavior exhibited by arbitrarily shaped inclusions, they also indicate that knowledge and the exploitation of such systems remains quite limited.

Finally, we provide a few remarks to place this work in context. The current results combined with previous data are important from both practical and fundamental points of view. Our approach is expected to be particularly useful to construct models of electromagnetic wave transport in complex systems, e.g., monolayer colloidal suspensions confined between narrowly spaced glass plates [32], where shape, roughness, and other morphological parameters all contribute to the macroscopic dielectric response. In many situations, deterministic models fail to capture the inherent topology of the heterostructure, and stochastic models are necessary. Recent work on random granular composite materials has shown interesting dielectric properties that can be directly related to the existence of randomness and connectedness of the boundaries [6,34–36]. While this approach is very powerful and has been applied to many systems, only numerical simulations are possible in general. In such cases, the analysis of the ensemble-averaged composite is often conducted using a Monte Carlo (MC) algorithm. A follow-on investigation of such MC simulations with irregularly shaped inclusions is in progress [36].

It should be borne in mind that the treatment should eventually be extended to metamaterials and artificial multilayered inclusions with desired functionality. This observation naturally suggests that other more "irregular" types of inclusion determined by topology optimization may also possess interesting depolarization properties [49–51]. Vast opportunities undoubtedly remain for applying principles of electrostatics to the practical design of dielectric heterostructures to provide novel functionality of these systems.

As mentioned in the Introduction, among the remaining interesting questions arising in granular heterostructures is the ability to predict DF with respect to size. In order for the expansions [Eqs. (4) and (5)] to make sense, the applied electric field is assumed to interact with the electric dipole moment of the system. Obviously, the range of validity of

this condition depends on composition. However, below a critical size limit, the exchange-coupling term is largely predominant over other energy contributions and the polarization mechanisms are expected to be largely dependent on interfacial layer preparation and annealing temperature [52]. Further studies should be conducted on nanocomposites with varying nanoscale particle sizes, but with other properties held constant to systematically investigate this effect. One key advantage of using magnetoelectric materials [53], e.g., multiferroics, lies in the extra degree of freedom available for tailoring these materials by coupling polarization and magnetization mechanisms, i.e., the possibility to manipulate the electric behavior by magnetic field and vice versa. Because properties and effects are classified according to the lowest multipole order of polarizability densities that is necessary to describe the property or effect [54], it is important to consider carefully the DF of magnetoelectric materials. Whereas the electric dipole approximation was an implicit assumption of our work, the magnetoelectric effect is of electric quadrupole-magnetic dipole order and thus it would be desirable to perform simulations that include a higher-order moment of the system. Furthermore, the results we presented here may have an impact to help develop theoretical approaches in the basic physics of surface-plasmon excitations occurring at metal (dielectric) interfaces [55] and in surface-enhanced Raman scattering [56]. We look forward to the day when artificial nanostructures can be designed by suitably combining numerical results with minimal experimental work.

ACKNOWLEDGMENT

The authors would like to acknowledge support from the Laboratoire d'Electronique et Systèmes de Télécommunications, Unité Mixte de Recherche CNRS 6616.

APPENDIX: DEPOLARIZATION FACTOR FOR A THREE-DIMENSIONAL CYLINDER OF FINITE LENGTH

As we noted in Sec. I, the inclusion shapes investigated can be considered as cross sections of infinite three-dimensional objects. For instance, the disk represents an infinite cylinder with its axis along z embedded in an infinite medium for which it is assumed that everything happens in the (x,y) plane and depends on (x,y) only. A few words of caution are in order here. While these cross sections are obviously two-dimensional structures, one cannot neglect the third dimension (or taking it equal to zero) from an electromagnetic-response standpoint. To substantiate this point, the depolarizing factor produced by a circular cylinder (Fig. 9) with finite thickness was calculated. The method of calculation we employed for this system is very similar to that developed in Sec. II B with appropriate physical boundary conditions. The main point of interest is to consider the dependence of the DF along the z axis as a function of the aspect ratio of the cylinder. Typical results are summarized in Table VIII. The general trend in Table VIII is that A in the z direction decreases with rising aspect ratio H/R, where H and R are the cylinder length and radius, respectively. It is instructive to consider the asymptotic behavior of the DF for very thin $(H/R \to 0)$ or very long $(H/R \to \infty)$ cylinders and compare with 1/2, which is the value of the DF of an infinite cylinder (discoidal inclusion in Sec. III A). The DF of a disk of negligible thickness is actually zero. In fact, since the full DF tensor is traceless, and the z component of a disk of negligible thickness is equal to one (fully depolarized), then the x and y components vanish). On the contrary, for the infinite cylinder, the z component is zero, so that the x and y components are both equal to 1/2 by symmetry. We found (not shown) that the calculations of the DF, in the direction of its major axis, for very elongated $(H/R \to \infty)$ inclusions are consistent with the results of Ref. [19], predicting a "universal curve," which is proportional to $(R/H)^2 \ln(H/R)$. They are also in agreement with similar observations re-

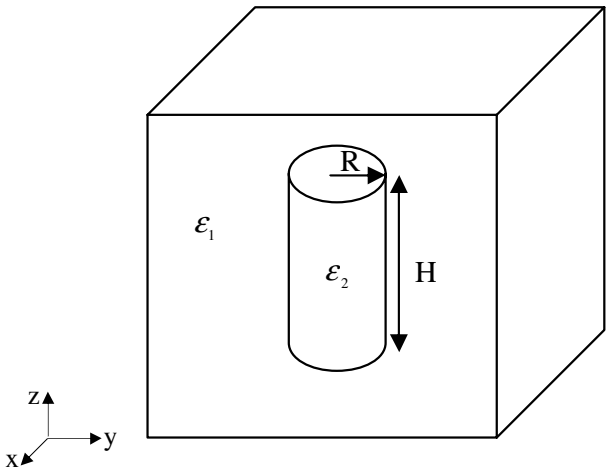

FIG. 9. Sketch of a three-dimensional circular cylinder where H and R are the cylinder length and radius, respectively, and Cartesian coordinate system.

TABLE VIII. The DF along the z axis as a function of the cylinder aspect ratio, H/R, where H and R are the cylinder length and radius, respectively (with reference to Fig. 9). The permittivity contrast is set to $\varepsilon_2/\varepsilon_1 = 20/2$.

	3D Cylinder (Fig. 9) $A\left(\frac{\varepsilon_2}{\varepsilon_1}=\frac{20}{2}\right)$	
	Approximation	
HR	1	2
1/10	0.840	0.855
1/5	0.701	0.713
1/2	0.512	0.526
1	0.407	0.451
2	0.198	0.202
5	0.097	0.099
10	0.053	0.051

ported for the demagnetizing factors for cylinders, i.e., Fig. 7 of Ref. [57], and the effective electromagnetic properties of composites containing elongated conducting inclusions [58].

We end with two additional remarks in relation to the present paper. First, it is to be emphasized that cylinders with other shapes of cross sections, e.g., ellipsoidal cross section, were tried and we obtained similar trends (not shown). Second, there is an analogy of the present results with the calculation of the demagnetizing factors for a series of dielectric columns [57]. The FE method was used in Ref. [57] and imposes the constraint that the magnetization is constant in each finite element. The scalar potential formalism was then used to solve the magnetostatic problem with standard magnetostatic boundary conditions in terms of the magnetostatic potential at the nodes of the finite elements. Although based on a different approach from that in Ref. [57], the interested reader may also consult Ref. [48] for a recent breakthrough in the exact determination of the demagnetization factors of arbitrary bodies by means of Fourier-space technique. Finally, we note that in recent years lithography, e.g., interference lithography combined with electrodeposition, magnetic characterization, and computational techniques have improved to the point that it is now possible to compare three-dimensional model predictions directly to experimental data gathered from individual cylindrical inclusions or arrays of cylindrical inclusions, revealing the effects of microstructure, interactions between the inclusions, and size variations on magnetic behavior [59].

[1] C. Brosseau and A. Beroual, Prog. Mater. Sci. **48**, 373 (2003).
[2] G. Bosi, F. E. Girouard, and V. V. Truong, J. Appl. Phys. **53**, 648 (1982).
[3] G. Bosi, J. Opt. Soc. Am. B **9**, 208 (1992).
[4] R. G. Barrera, M. del Castillo-Mussot, G. Monsivais, P. Villaseñor, and W. L. Mochán, Phys. Rev. B **43**, 13819 (1991); R. G. Barrera, G. Monsivais, and W. L. Mochán, Phys. Rev. B **38**, 5371 (1988).
[5] E. C. Chan, and J. P. Marton, J. Appl. Phys. **45**, 5004 (1974).
[6] A. H. Sihvola, *Electromagnetic Mixing Formulas and Applications* (IEE Publishing, London, 1999).
[7] S. Torquato, *Random Heterogeneous Materials: Microstructure and Macroscopic Properties* (Springer, New York, 2002).
[8] G. W. Milton, *The Theory of Composites* (Cambridge University Press, Cambridge, 2002).
[9] A. Lakhtakia and N. Lakhtakia, Optik (Stuttgart) **109**, 140 (1998).
[10] W. Weiglhofer, J. Phys. A **31**, 7191 (1998).
[11] A. Yaghjian, Proc. IEEE **68**, 248 (1980). See also C. T. Tai and A. Yaghjian, *ibid.* **69**, 282 (1981).
[12] E. J. Garboczi and J. F. Douglas, Phys. Rev. E **53**, 6169 (1996); M. L. Mansfield, J. F. Douglas, and E. J. Garboczi, *ibid.* **64**, 061401 (2001); J. F. Douglas and E. J. Garboczi, Adv. Chem. Phys. **91**, 85 (1991).
[13] A. Sihvola, J. Venermo, and P. Ylä-Oijala, Microwave Opt. Technol. Lett. **41**, 245 (2004).
[14] A. Mejdoubi and C. Brosseau, J. Appl. Phys. **99**, 063502 (2006).
[15] A. Mejdoubi and C. Brosseau, Phys. Rev. E **73**, 031405 (2006).
[16] A. Mejdoubi and C. Brosseau, J. Appl. Phys. (to be published).
[17] S. Berthier, K. Driss-Khojda, and J. Lafait, Europhys. Lett. **4**, 1415 (1987).
[18] X. C. Zeng, P. M. Hui, and D. Stroud, Phys. Rev. B **39**, 1063 (1989); X. C. Zheng, P. M. Hui, D. J. Bergman, and D. Stroud, *ibid.* **39**, 13224 (1989).
[19] L. Landau and E. Lifshitz, *Electrodynamics of Continuous Media*, 2nd ed. (Pergamon Press, Oxford, 1984).
[20] J. J. H. Wang, IEEE Trans. Antennas Propag. **AP-30**, 463 (1982).
[21] I. V. Lindell, *Methods for Electromagnetic Field Analysis* (Oxford University Press, Oxford, UK, 1995).
[22] See, for example, B. K. P. Scaife, *Principles of Dielectrics* (Clarendon Press, Oxford, 1998).
[23] S.-W. Lee, J. Boersma, C.-L. Law, and G. A. Deschamps, IEEE Trans. Antennas Propag. **AP-28**, 311 (1980).
[24] J. van Bladel, *Singular Electromagnetic Fields and Sources* (IEEE, New York, 1995).
[25] W. F. Brown, J. Chem. Phys. **23**, 1514 (1955).
[26] S. Torquato, J. Appl. Phys. **58**, 3790 (1985).
[27] G. Pólya and G. Szegö, *Isoperimetric Inequalities in Mathematical Physics* (Princeton University Press, Princeton, NJ, 1951).
[28] H. Ammari and H. Kang, Contemporary Math. (to be published).
[29] M. Sahimi, *Heterogeneous Materials I. Linear Transport and Optical Properties* (Springer, New York, 2003).
[30] A. K. Sen and S. Torquato, Phys. Rev. B **39**, 4504 (1989).
[31] S. P. Friedman and D. A. Robinson, Water Resour. Res. **38**, 1236 (2002).
[32] K. Asami, J. Phys. D **39**, 492 (2006).
[33] R. Elghanian, J. Storhoff, R. C. Mucic, R. L. Letsinger, and C. A. Mirkin, Science **277**, 1078 (1997).
[34] V. Myroshnychenko and C. Brosseau, Phys. Rev. E **71**, 016701 (2005).
[35] V. Myroshnychenko and C. Brosseau, J. Appl. Phys. **97**, 044101 (2005).
[36] V. Myroshnychenko and C. Brosseau (unpublished).
[37] W. Lamb, D. M. Wood, and N. W. Ashcroft, Phys. Rev. B **21**, 2248 (1980).
[38] D. J. Bergman and D. Stroud, Solid State Phys. **46**, 147 (1992).
[39] For background reading, we refer the reader to O. C. Zienkiewicz and R. L. Taylor, *The Finite-Element Method* (McGraw-Hill, New York, 1994). See also J. Jin, *The Finite-Element in Electromagnetics* (Wiley, New York, 1993).
[40] G. Y. Lyubarskii, *Application of Group Theory in Physics* (Pergamon Press, New York, 1960).
[41] H. E. Stanley, *in Fractals and Disordered Systems*, edited by A. Bunde and S. Havlin (Springer-Verlag, Berlin, 1991). See also J. Feder, *Fractals* (Plenum, New York, 1988).
[42] D. Gershon, J. P. Calame, and A. Birnboim, J. Appl. Phys. **89**,

8117 (2001); A. Birnboim, J. Calame, and Y. Carmel, *ibid.* **85**, 1 (1999); J. P. Calame, A. Birman, Y. Carmel, D. Gershon, B. Levush, A. A. Sorokin, V. E. Semenov, D. Dadon, L. P. Martin, and M. Rosen, *ibid.* **80**, 3992 (1996).

[43] E. Tuncer, Turk. J. Phys. **27**, 121 (2003).

[44] M. Beleggia, M. De Graef, and Y. T. Miller, J. Phys. D **39**, 891 (2006).

[45] S. B. Jones and S. P. Friedman, Water Resour. Res. **36**, 2821 (2000).

[46] E. C. Stoner, Philos. Mag. **36**, 803 (1945).

[47] J. A. Osborne, Phys. Rev. **67**, 351 (1945).

[48] S. Tandon, M. Beleggia, Y. Zhu, and M. de Graef, J. Magn. Magn. Mater. **271**, 27 (2004); **271**, 9 (2004).

[49] A. Cherkaev, *Variational Methods for Structural Optimization*, Appl. Math. Sciences Vol. 140 (Springer, New York, 2000).

[50] S. Torquato, S. Hyun, and A. Donev, Phys. Rev. Lett. **89**, 266601 (2002).

[51] G. Allaire, *Shape Optimization by the Homogenization Method* (Springer-Verlag, New York, 2002).

[52] C. Brosseau, J. Ben-Youssef, P. Talbot and A.-M. Konn, J. Appl. Phys. **93**, 9243 (2003); C. Brosseau and P. Talbot, IEEE Trans. Dielectr. Electr. Insul. **11**, 819 (2004); S. Mallegol, C. Brosseau, P. Queffelec, and A.-M. Konn, Phys. Rev. B **68**, 174422 (2003); C. Brosseau, S. Mallegol, P. Queffelec, and J. Ben Youssef, *ibid.* **70**, 092401 (2004); C. Brosseau and P. Talbot, J. Appl. Phys. **97**, 104325 (2005).

[53] M. I. Bichurin, V. M. Petrov, and G. Srinivasan, Phys. Rev. B **68**, 054402 (2003); M. I. Bichurin, D. A. Filippov, V. M. Petrov, V. M. Laletsin, N. Paddubnaya, and G. Srinivasan, *ibid.* **68**, 132408 (2003).

[54] R. E. Raab and O. L. de Lange, *Multipole Theory in Electromagnetism* (Clarendon, Oxford, 2005).

[55] S. A. Maier and H. A. Atwater, J. Appl. Phys. **98**, 011101 (2005).

[56] H. Xu, E. J. Bjerneld, M. Kall, and L. Borjesson, Phys. Rev. Lett. **83**, 4357 (1999); S. Nie and S. R. Emory, Science **275**, 1102 (1997).

[57] D.-X. Chen, J. A. Brug, and R. B. Goldfarb, IEEE Trans. Magn. **27**, 3601 (1991).

[58] A. N. Lagarkov and A. K. Sarychev, Phys. Rev. B **53**, 6318 (1996).

[59] C. A. Ross, M. Hwang, M. Shima, J. Y. Cheng, M. Farhoud, T. A. Savas, H. I. Smith, W. Schwarzacher, F. M. Ross, M. Redjdal, and F. B. Humphrey, Phys. Rev. B **65**, 144417 (2002).